Material-Stiffening Suppresses Elastic Fingering and Fringe Instabilities

Shaoting Lin[1], *Yunwei Mao*[1], *Hyunwoo Yuk*[1], *Xuanhe Zhao*[1,2 *]

[1.] *Department of Mechanical Engineering, Massachusetts Institute of Technology, Cambridge, MA 02139, USA;* [2.] *Department of Civil and Environmental Engineering, Massachusetts Institute of Technology, Cambridge, MA 02139, USA*

* To whom correspondence should be addressed. Email: zhaox@mit.edu

Abstract

When a confined elastic layer is under tension, undulations can occur at its exposed surfaces, giving the fingering or fringe instability. These instabilities are of great concern in the design of robust adhesives, since they not only initiate severe local deformations in adhesive layers but also cause non-monotonic overall stress vs. stretch relations of the layers. Here, we show that the strain stiffening of soft elastic materials can significantly delay and even suppress the fringe and fingering instabilities, and give monotonic stress vs. stretch relations. Instability development requires local large deformation, which can be inhibited by material-stiffening. We provide a quantitative phase diagram to summarize the stiffening's effects on the instabilities and stress vs. stretch relations in confined elastic layers. We further use numerical simulations and experiments to validate our findings.

Keywords: Fingering instability, Fringe instability, Confined layers, Strain stiffening, Adhesives

Material-Stiffening Suppresses Elastic Fingering and Fringe Instabilities

1. Introduction

Confined elastic layers are ubiquitous in nature such as mussel plagues, tendons and ligaments (Benjamin et al., 2006; Desmond et al., 2015; Waite et al., 2005) and widely adopted in engineering applications such as insulators, sealants, artificial joints, and versatile adhesives (Biggins et al., 2013; Creton and Ciccotti, 2016; Liu et al., 2017; Shull, 2002; Yuk et al., 2017). When a confined elastic layer is under tension, fringe instability (Lin et al., 2016) or fingering instability (Biggins et al., 2013; Shull et al., 2000) can form at its exposed surfaces, leading to various modes of failures including interfacial detachment and cohesive fracture in relevant structures (Chaudhury et al., 2015; Crosby et al., 2000; Zhao et al., 2006). The approaches to suppress these instabilities are of great importance to the design of robust adhesives (Yuk et al., 2016a), which nevertheless have not been explored so far.

Here, we show that both fringe instability and fingering instability can be suppressed if the confined layer stiffens significantly at moderate stretches. We adopt a Gent solid (Gent, 1996) with shear modulus μ and limit of the strain invariant J_m to model the mechanical behavior of stiffening layers under tension. From combined experiments and simulation, we identify two critical values for J_m of a material: J_{mono} below which the tensile stress vs. stretch relation of a confined layer is monotonic, although either fringe or fingering instability may set in the layer; and J_{inst} below which both fringe instability and fingering instability are fully suppressed. To further experimentally validate the suppression of both fringe and fingering instabilities in a stiffening layer, we perform a set of controlled experiments by applying tensile load on an Ecoflex layer and a hydrogel layer, representing stiffening material and non-stiffening material respectively. The understanding on suppression of elastic instabilities in a confined strain

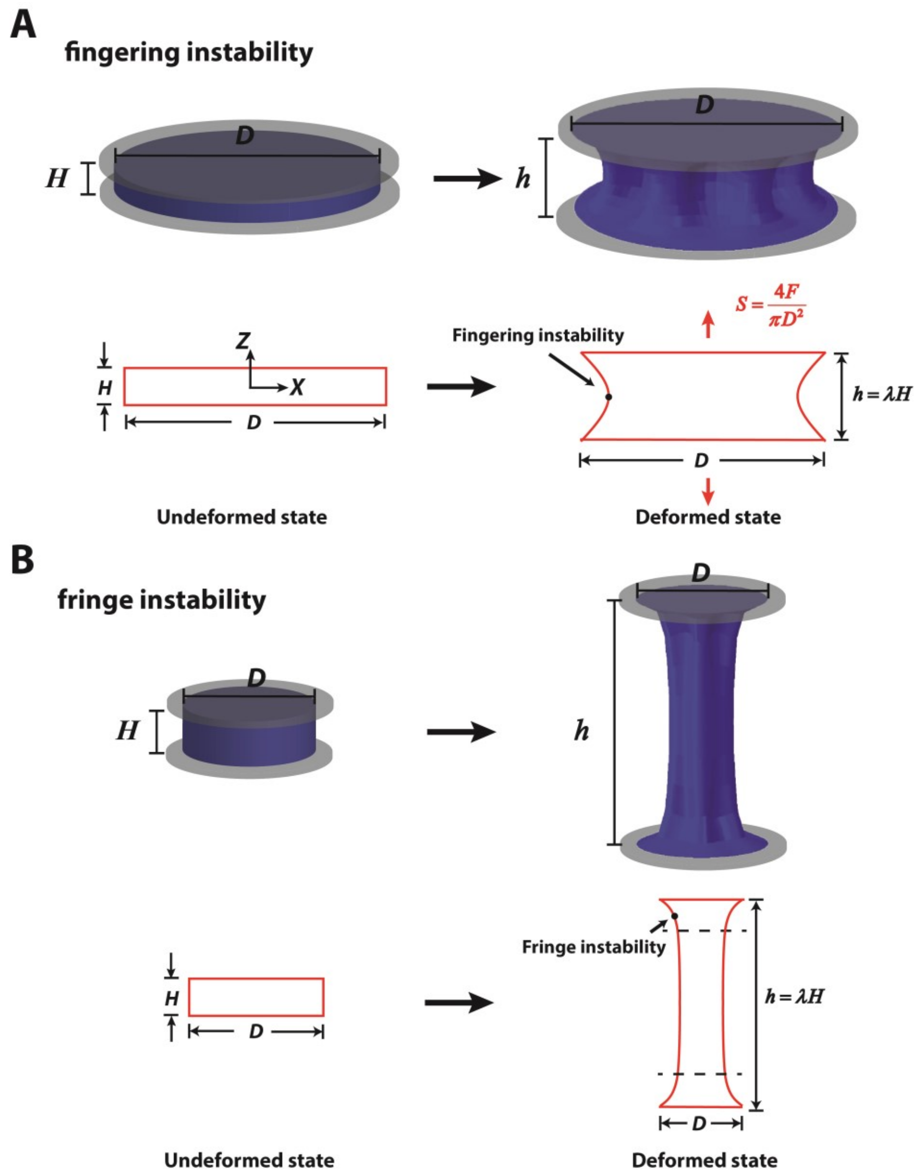

Figure 1. a) Schematic of the formation of fingering instabilities in elastic layers with diameter of D and thickness of H. Fingering instability initiates at the middle-plane of the elastic layer. b) Schematic of the formation of fringe instabilities in elastic layers with diameter of D and thickness of H. Fringe instability initiates at the plane close to the fringe portion of the elastic layer. The aspect ratio of the layer is defined as $\alpha = D / H$.

stiffening layer can serve as a guideline for the design of robust adhesives for engineering applications (Yuk et al., 2016a; Yuk et al., 2016b). Moreover, it may also elucidate one possible reason why stiffening layers such as cartilage, ligament and mussel thread (Sharma et al., 2016; Silverman and Roberto, 2007) are adopted in nature.

2. Formulation of the problem

As illustrated in **Fig. 1**, we focus on an elastic layer of cylindrical shape with height H and diameter D at the undeformed state. A tensile force F is applied on the layer to elongate the layer to the current height h. The applied nominal stress S and the applied stretch λ is defined as:

$$S = \frac{4F}{\pi D^2} \ , \quad \lambda = \frac{h}{H} . \tag{1}$$

Geometrically, the cylindrical elastic layer in the undeformed state occupies a region $0 \le R \le D/2$, $0 \le \Theta < 2\pi$, and $-H/2 \le Z \le H/2$. The corresponding dimensionless parameters are defined as $\bar{R} = \frac{R}{D/2}$ and $\bar{Z} = \frac{Z}{H/2}$ with $\bar{R} \in [0,1]$ and $\bar{Z} \in [-1,1]$. The deformation gradient of the elastic layer reads as $\mathbf{F} = \mathbf{1} + \nabla \mathbf{u}$ with $\mathbf{u}(R,\Theta,Z) = u_R \mathbf{e_R} + u_\Theta \mathbf{e_\Theta} + u_Z \mathbf{e_Z}$ being the displacement vector of a point initially at (R,Θ,Z), where u_R, u_Θ and u_Z are radial displacement, hoop displacement, and axial displacement, respectively. The elastic layer is taken as a Gent solid (Gent, 1996), with the free energy reading as:

$$\psi = -\frac{\mu J_m}{2} \ln\left(1 - \frac{J_1}{J_m}\right) + \kappa \ln J , \tag{2}$$

where μ is the shear modulus, κ is the bulk modulus, $J = \det(\mathbf{F})$, the strain invariant $J_1 = \mathrm{tr}\left(\bar{\mathbf{F}}\bar{\mathbf{F}}^{\mathrm{T}}\right) - 3$ with $\bar{\mathbf{F}} = J^{-1/3}\mathbf{F}$ and J_m is the material constant which identifies the limiting value of J_1. We set the elastocapillary length of the layer to be much smaller than the macroscopic dimensions of the sample (i.e. D and H), therefore having negligible effects on the emergence of elastic instabilities. Moreover, we set κ / μ as large as 2000, thus the slight incompressibility does not have observable effect on emergence of elastic instabilities. The parameters affecting the mechanical behavior of the elastic layer are: layer's aspect ratio $\alpha = D/H$ and material constants μ and J_m. The material particles in the layer satisfy the stress equilibrium by $\mathrm{Div}\,\mathbf{S} = \mathbf{0}$, with the nominal stress tensor $\mathbf{S} = \frac{\mu J_m}{J_m - J_1}\left[J^{-2/3}\mathbf{F} - \frac{1}{3}\mathrm{tr}\left(\overline{\mathbf{F}}\overline{\mathbf{F}}^{\mathrm{T}}\right)\mathbf{F}^{-\mathrm{T}} \right] + \kappa \ln(J)\mathbf{F}^{-\mathrm{T}}$ and $\overline{\mathbf{F}} = J^{-1/3}\mathbf{F}$. The displacement boundary conditions are: $u_R\left(\overline{Z} = \pm 1\right) = 0$, $u_\Theta\left(\overline{Z} = \pm 1\right) = 0$, $u_Z\left(\overline{Z} = 0\right) = 0$ and $u_Z\left(\overline{Z} = 1\right)$ is the imposed displacement on the top surface of the layer.

We use the commercial finite element software Abaqus/Explicit by writing a VUMAT subroutine to simulate the deformation of elastic layer and capture the onset of instabilities. The ratio between bulk modulus κ and shear modulus μ is set as $\kappa/\mu = 2000$ for all cases in this paper, to approximate the incompressibility of the layer. The type of the element is taken as C3D8 and the mesh size is taken as ~ 1/10 of the smallest feature dimension.

When the elastic layer is under tension, the exposed surface of the layer initially deforms into a parabolic shape. When the applied stretch reaches a critical value λ_c (or the applied nominal stress reaches S_c), undulations emerge at the exposed surfaces of the layer, giving fringe instability or fingering instability (Biggins et al., 2013; Lin et al., 2017). We take the vertical location that gives the highest undulation amplitude $\overline{Z} = \overline{Z}_0$ as the location where the undulations initiate in simulation.

3. Effects of Material Stiffening on fingering and fringe instabilities

In previous study on non-stiffening materials (i.e. $J_m \to \infty$), we find the aspect ratio $\alpha = D/H$ determines the selection of the mode of instability (Lin et al., 2017). As shown in **Fig. 1**, for the samples with large aspect ratio α in which fingering instability sets in, the instability initiates at the middle section of the exposed meniscus (i.e. $\bar{Z}_0 = 0$) ; while for the samples with small aspect ratio α, the instability initiates at the fringe portion of the exposed meniscus (i.e. $\bar{Z}_0 \neq 0$), giving fringe instability. The critical aspect ratio between fringe instability and fingering

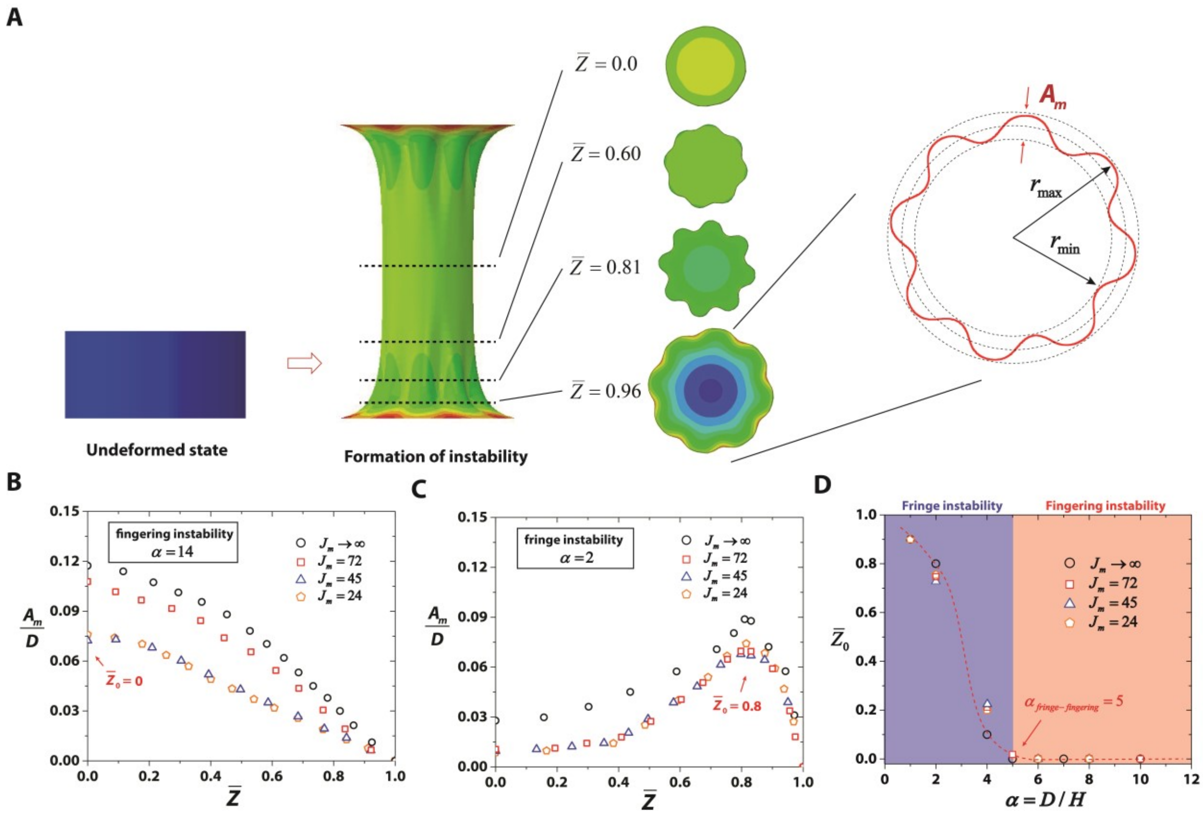

Figure 2. a) Illustration of the amplitude of undulations at various vertical locations. b) The normalized amplitude A_m / D versus vertical location $\bar{Z}$ at the onset of fingering instability in the layers with large aspect ratio (i.e. $\alpha = 14$) for both non-stiffening layers (i.e. $J_m \to \infty$) and stiffening layers with various limits of strain invariant J_m. The vertical location with maximum amplitude identifies the vertical plane where undulations initiate (i.e. $\bar{Z}_0 = 0$), at middle-plane of the layer. c) The normalized amplitude A_m / D versus vertical location $\bar{Z}$ at the onset of fringe instability in the layers with small aspect ratio (i.e. $\alpha = 2$) for both non-stiffening layers (i.e. $J_m \to \infty$) and stiffening layers with various limits of strain invariant J_m. The vertical location with maximum amplitude identifies the vertical plane where undulations initiate (i.e. $\bar{Z}_0 = 0.8$), close to fringe portion. d) The vertical plane where undulations initiate for the layers with various aspect ratios and various limits of strain invariant. For the samples with large aspect ratio α in which fingering instability sets in, the instability initiates at the middle section of the exposed meniscus (i.e. $\bar{Z}_0 = 0$) ; while for the samples with small aspect ratio α, the instability initiates at the fringe portion of the exposed meniscus (i.e. $\bar{Z}_0 \neq 0$), giving fringe instability.

instability has been identified as $\alpha_{fringe-fingering} = 5$ for non-stiffening materials (Lin et al., 2017). Here, we further investigate the effect of material-stiffening on $\alpha_{fringe-fingering}$ by performing a set of numerical simulations for the samples with various aspect ratios α ranging from 1 to 10 and various limits of the strain invariant (i.e. $J_m = 24$, $J_m = 45$ and $J_m = 72$). We extract the contour of exposed surface at each vertical location of the layer at the onset of instabilities as shown in **Fig. 2a**. The difference between the maximum radius $r_{\max}$ and the minimum radius $r_{\min}$ defines the amplitude of the contour A_m. We further plot the normalized amplitude A_m / D versus vertical location $\bar{Z}$ in the layer. As shown in **Fig. 2b**, for the layers with large aspect ratio (i.e. $\alpha = 14$) in which fingering instability sets in, the vertical location that gives the maximum amplitude is at the middle plane (i.e. $\bar{Z}_0 = 0$) for the layers in both non-stiffening layers and stiffening layers with

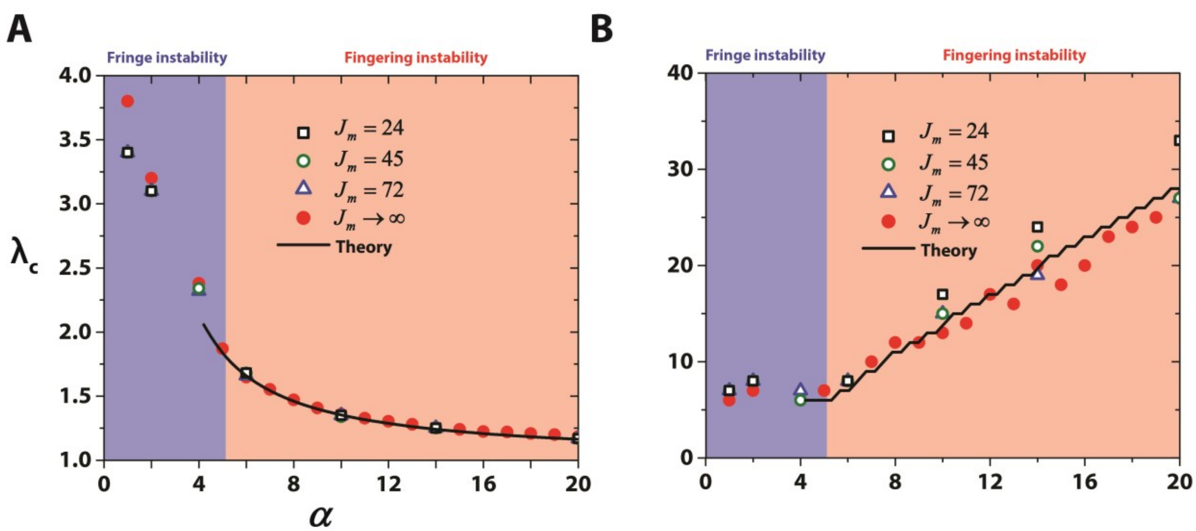

Figure 3. Theoretical and simulation results on the critical points of fingering instability and fringe instability. a) Comparison of the critical stretch λ_c for the onset of instabilities between theory and simulation. b) Comparison of the critical mode number ω_c between theory and simulation. Solid line denotes the theoretical results for non-stiffening layers (i.e. $J_m \to \infty$). Solid circular dots denote simulations results non-stiffening layers (i.e. $J_m \to \infty$). Hollow square dots, circular dots and triangular dots denote simulation results for stiffening layers with $J_m = 24$, $J_m = 45$ and $J_m = 72$.

$J_m = 24$, $J_m = 45$ and $J_m = 72$. As shown in **Fig. 2c**, for the layers with small aspect ratio (i.e. $\alpha = 2$) in which fringe instability sets in, the vertical location that gives the maximum amplitude is at the plane $\bar{Z}_0 = 0.8$ for the layers in both non-stiffening layers and stiffening layers with $J_m = 24$, $J_m = 45$ and $J_m = 72$. We summarize the vertical location that gives the maximum amplitude at the onset of instabilities in both stiffening layers and non-stiffening layers. As shown in **Fig. 2d**, the limit of the strain invariant J_m does not affect the critical aspect ratio between fringe instability and fingering instability significantly, which is the same as that in a non-stiffening layer (i.e. $\alpha_{fringe-fingering} = 5$).

We further explore the effect of material-stiffening on the onset of instabilities in elastic layers. In previous study on non-stiffening materials (i.e. $J_m \to \infty$), we derive the analytical solution of the deformation field and predict the critical stretch λ_c and the critical number of undulations ω_c for the onset of instabilities in elastic layers. We summarize the theoretical analysis for the onset of instabilities in non-stiffening materials in **Appendix**. With the increase of the layer's aspect ratio α, the critical stretch λ_c decreases while the critical number of undulations ω_c increases. We first perform a set of simulations for the layers with moderate J_m (i.e. $J_m = 24$, $J_m = 45$ and $J_m = 72$). As shown in **Fig. 3**, material-stiffening has negligible effect on the critical stretch λ_c and slightly increases the critical number of undulations ω_c.

Next, we study the effect of material stiffening on the suppression of both fingering and fringe instabilities. We first study fingering instability (in the samples with $\alpha = 6$) for both stiffening and non-stiffening materials. As shown in **Fig. 4a** and **Fig. 4c**, for a non-stiffening layer

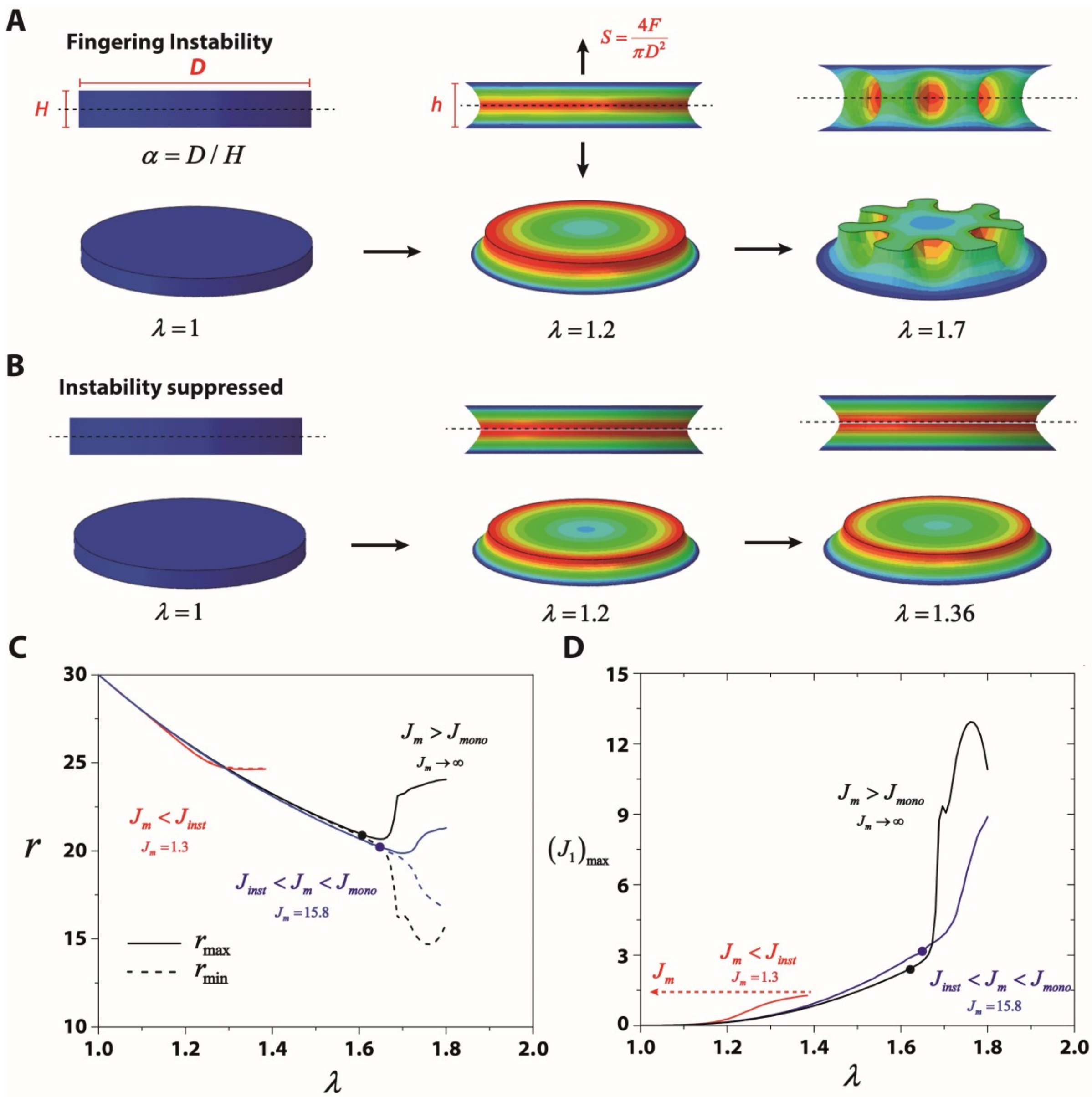

Figure 4. Suppression of fingering instability in the sample with aspect ratio of $\alpha = 6$. a) Fingering instability emerges in a neo-Hookean layer. b) Fingering instability suppressed in a Gent solid with the limit of the strain invariant $J_m = 1.3$. c) The radius of the outer surface at the middle plane of the layer where undulations initiate and d) the maximum strain invariant $(J_1)_{max}$ at the plane where instability initiates. Dots represent the onset of fingering instabilities.

(i.e. $J_m \to \infty$), as the applied stretch reaches $\lambda_c = 1.62$, the radius of the external surface r at the middle plane where undulations initiate (i.e. $\bar{Z}_0 = 0$) bifurcates, giving the fingering instability. Right after the onset of fingering instability, the maximum strain invariant $(J_1)_{\max}$ at the plane where instability initiates (i.e. $\bar{Z}_0 = 0$) increases dramatically, corresponding to the first-order transition of fingering instability (Biggins et al., 2013) (see **Fig. 4d**). In contrast, for a stiffening layer with moderate J_m (e.g. $J_m = 15.8$), the bifurcation of the radius at the middle plane is partially suppressed, manifested by the decreasing undulation amplitude $r_{\max} - r_{\min}$ (see **Fig. 4c**). In addition, the maximum first strain invariant $(J_1)_{\max}$ in the layer increases less steeply than that of the non-stiffening layer. For an elastic layer which stiffens at early stretches (e.g. $J_m = 1.3$), fingering instability can be fully suppressed and no bifurcation can be observed even when the maximum first strain invariant within the layer $(J_1)_{\max}$ approaches the limit of J_m (see **Fig. 4b**, **Fig. 4c** and **Fig. 4d**). We next study fringe instability (in the samples with $\alpha = 1$) for both stiffening and non-stiffening materials. As illustrated in **Fig. 5a**, fringe instability emerges in a non-stiffening layer when the applied stretch reaches $\lambda_c = 4$, corresponding to the bifurcation of the radius of the outer surface initiating at the plane of $\bar{Z}_0 = 0.9$ (see **Fig. 5a**). While for the stiffening layer with $J_m = 9$, no bifurcation occurs at the exposed surface even when the maximum first strain invariant $(J_1)_{\max}$ at the plane where instability initiates (i.e. $\bar{Z}_0 = 0.9$) increases up to the limit of J_m (see **Fig. 5b**, **Fig. 5c** and **Fig. 5d**).

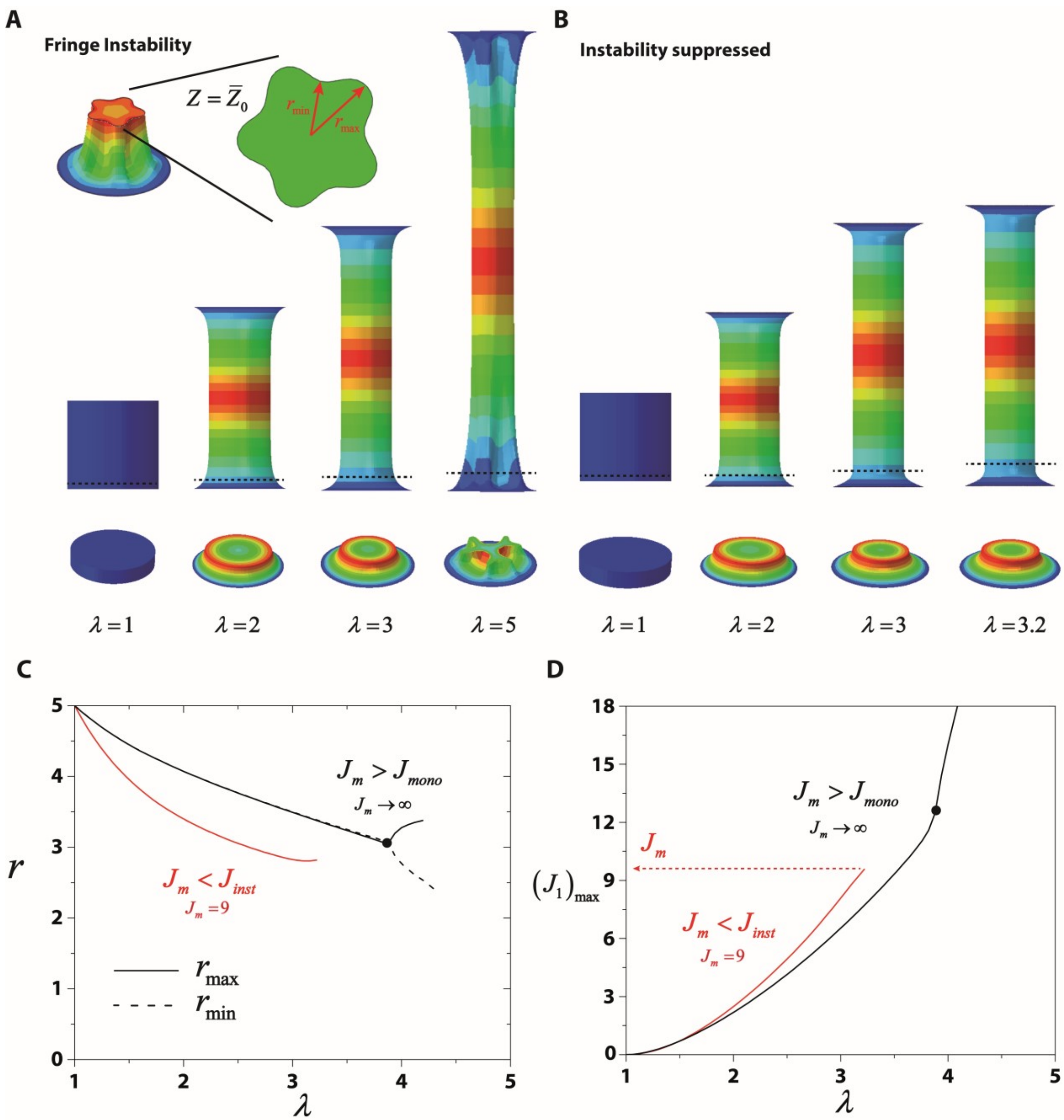

Figure 5. Suppression of fringe instability in the sample with aspect ratio of $\alpha = 1$. a) Fringe instability emerges in a neo-Hookean layer. b) Fringe instability suppressed in a Gent solid with the limit of the strain invariant $J_m = 9$. c) The radius of the outer surface at the plane $\bar{Z}_0 = 0.9$ where undulations initiate and d) the maximum first strain invariant $(J_1)_{\max}$. Dots represent the onset of fringe instabilities.

As shown in **Fig. 4** and **Fig. 5**, both fingering instability and fringe instability can be suppressed in elastic layers with early stiffening. To identify the critical limit of the first strain invariant J_{inst} below which fingering instability (or fringe instability) can be fully suppressed, we perform a set of simulations with decreasing J_m and varying α. As shown in **Fig. 6**, the maximum strain invariant $(J_1)_{\max}$ of the layer at the plane where instability initiates is nearly constant for the layer with moderate J_m, while slightly increases and approaches the limit of the strain invariant J_m (the dashed line in **Fig. 6**) when J_m decreases. When J_m further decreases to a critical limit of the strain invariant J_{inst} (see the marked cross points in **Fig. 6**), instabilities are fully suppressed. It is also shown that the critical limit of the strain invariant J_{inst} decreases with the increase of the layer's aspect ratio α.

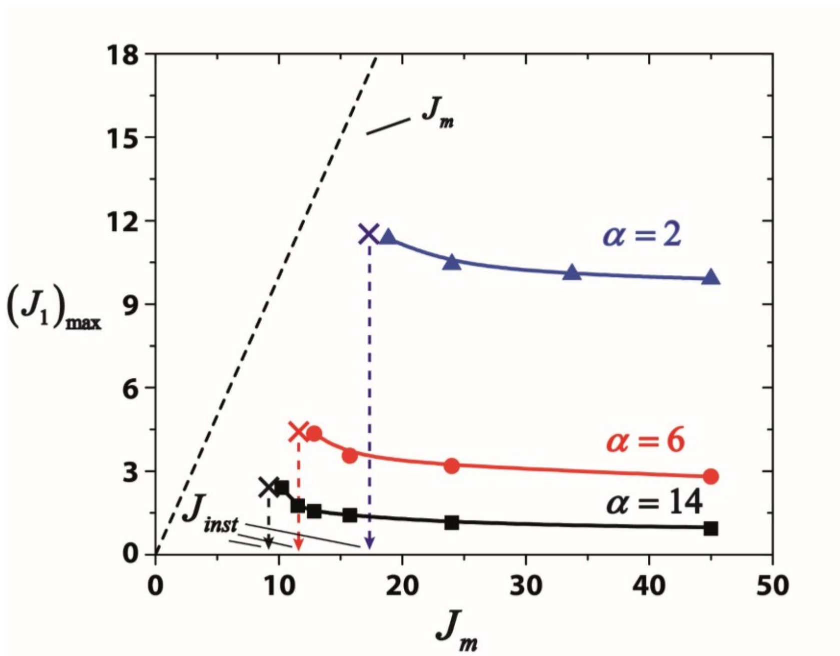

Figure 6. The maximum strain invariant $(J_1)_{\max}$ at the plane where instability initiates with various limit of first strain invariant J_m and aspect ratio of $\alpha = 2$, $\alpha = 6$ and $\alpha = 14$ at the onset of instabilities.

4. Effects of Material Stiffening on stress vs stretch relation

The applied nominal stress-stretch curve of a confined elastic layer under tension has been of great interests in the design of robust adhesives. It has been reported that, for a non-stiffening layer, the stress-stretch curve is monotonic for fringe instability in the samples with small aspect ratios (i.e. $\alpha < 5$); non-monotonic for fingering instabilities in the samples with large aspect ratios (i.e. $\alpha > 5$) (Lin et al., 2017). The non-monotonic stress-stretch relation in general is not preferred in adhesives, since it can cause catastrophic failures of the adhesives under increasing tensile stress. In this section, we will show that material-stiffening can change stress vs. stretch relation from non-monotonic to monotonic.

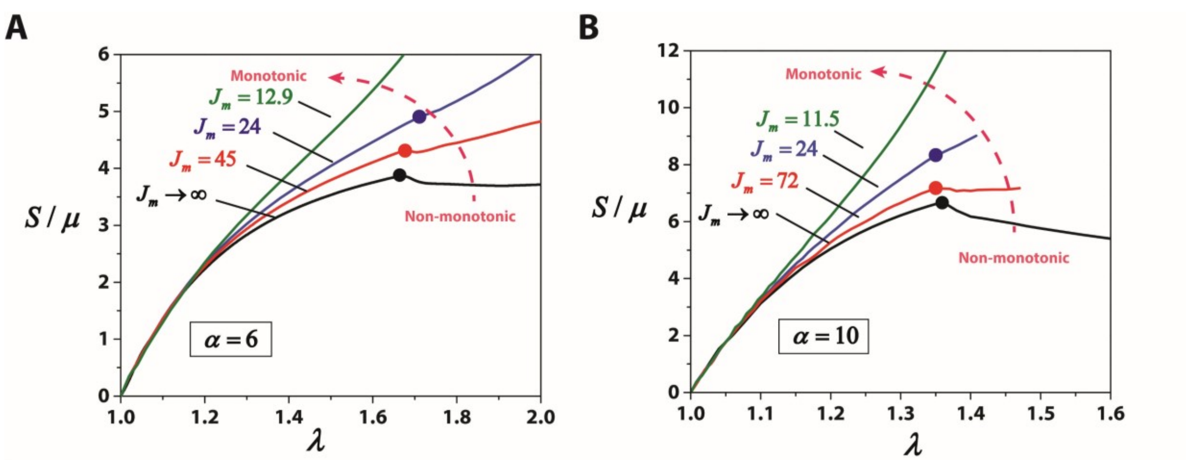

Figure 7. The stress-stretch curves for the sample with a) aspect ratio of $\alpha = 6$ and b) $\alpha = 10$. Dots represent the onset of fingering instabilities.

As shown in **Fig. 7a** and **Fig. 7b**, both layers with aspect ratio of $\alpha = 6$ and $\alpha = 10$ show non-monotonic stress vs. stretch relation for non-stiffening layer (i.e. $J_m \to \infty$) and the onset of fingering instability corresponds to the maximum applied stress. With the decrease of J_m, the normalized nominal stress S/μ increases and the stress vs. stretch relation transits from non-monotonic to monotonic in both layers. For the layer which stiffens at moderate stretches (e.g. $J_m = 24$ and $J_m = 45$ for $\alpha = 6$, $J_m = 24$ and $J_m = 72$ for $\alpha = 10$), the onset of fingering instability is corresponding to a kink of the stress-stretch curve while the stress keeps increasing. For the layers with early stiffening (e.g $J_m = 12.9$ for $\alpha = 6$, $J_m = 11.5$ for $\alpha = 10$), instabilities are shown to be fully suppressed and stress monotonically increases with the applied stretch. The transition of the stress vs. stretch relations from non-monotonic to monotonic gives the other critical limit of the strain invariant J_{mono}, below which the tensile stress vs. stretch relation of a confined layer is monotonic. As shown in **Fig. 8**, we summarize J_{mono} for the layers with the aspect ratio from 5 to 20.

5. Phase diagram for the suppression of instabilities in confined layers

In **Section 3**, we first identify the critical aspect ratio between fringe instability and fingering instability $\alpha_{fringe-fingering}$ and we further show the critical limit of first strain invariant J_{inst} below which both fringe instability and fingering instability are fully suppressed. In **Section 4**, we identify the other critical limit of first strain invariant J_{mono}, below which the tensile stress vs. stretch relation of a confined layer is monotonic. In this section, we summarize the results in previous sections and further construct a phase diagram in the plot of aspect ratio α and limit of the strain invariant J_m, elucidating the effect of material-stiffening on selection of modes and suppression of both fringe and fingering instabilities. As shown in **Fig. 8**, for a layer with early stiffening (i.e. $J_m < J_{inst}$), there is no fringe instability or fingering instability setting in. For a layer with moderate stiffening (i.e. $J_{inst} < J_m < J_{mono}$), undulations can initiate at the exposed surface of the layer and the applied stress monotonically increases with the applied stretch. For a layer which shows negligible stiffening (i.e. $J_m > J_{mono}$), the stress vs. stretch relation applied on the layer is non-monotonic and the onset of the instability (i.e. fingering instability) is correlated with the point of maximum stress. The phase diagram can serve as a guideline on selection of the mode of instability and monotonicity of stress vs. stretch relation.

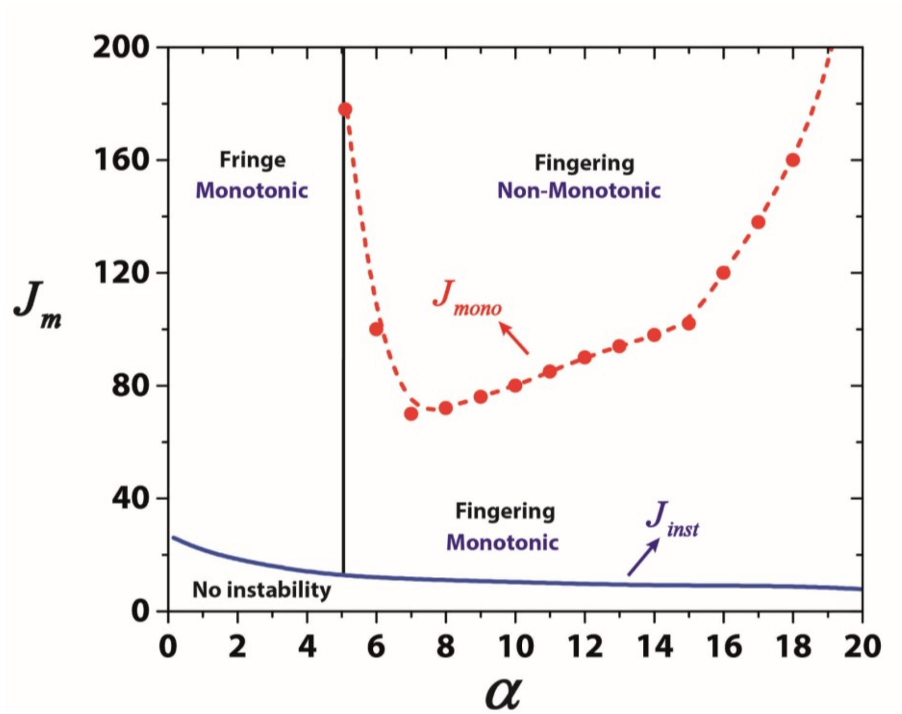

Figure 8. A phase diagram elucidating the suppression of fringe or fingering instabilities and the stress vs. stretch relation in confined elastic layers with respect to layer's aspect ratio α and limit of the strain invariant J_m.

6. Experimental validations

To validate the suppression of both fringe and fingering instabilities in experiment, we chose Ecoflex rubber and Polyacrylamide hydrogel as the representative stiffening solid and non-stiffening solid, respectively. The Ecoflec rubber is fabricated by mixing the Ecoflex 00-30 (Smooth on) with the ratio of 1:1. The polyacrylamide hydrogel consists of 12 wt% acrylamide (AAm), 2 wt% alginate and 500μL 0.23 wt% N,N'-Methylenebisacrylamide in 10 ml total solution. The detailed fabrication method is described in our previous papers (Lin et al., 2017). To measure the shear modulus μ and limit of the strain invariant J_m, we make dog-bone samples, performing uniaxial tensile tests. The measured shear modulus μ is 15 kPa and 1.1 kPa for Ecoflex rubber and polyacrylamide hydrogel, respectively. The limit of the strain invariant J_m for Ecoflex rubber and polyacrylamide hydrogel are measured to be 30 and 270, respectively. Recalling the phase diagram in **Fig. 8**, the limit of the strain invariant for Ecoflex is much lower than J_{mono} (i.e. $J_{mono} = 100$ for $\alpha = 6$) but slightly higher than J_{inst} (i.e. $J_{inst} = 18.9$ for $\alpha = 2$ and $J_{inst} = 11.5$ for $\alpha = 6$); while that for hydrogel is much larger than both J_{mono} (i.e. $J_{mono} = 100$ for $\alpha = 6$) and J_{inst} (i.e. $J_{inst} = 18.9$ for $\alpha = 2$ and $J_{inst} = 11.5$ for $\alpha = 6$).

As shown in **Fig. 9a**, for the samples with aspect ratio of $\alpha = 2$, fringe instability forms at the critical stretch of $\lambda_c = 3.9$ and the critical stress of $S_c = 3.8$ in hydrogel sample as reported in our previous work (Lin et al., 2016). While for the rubber sample with the identical dimensions, it deforms with uniform shrinkage and the applied normalized nominal stress S / μ increase dramatically (see **Fig. 9b**). There are negligible fringe undulations even when the applied stretch approaches the limiting locking stretch. We further perform a pair of controlled experiments for the samples with aspect ratio of $\alpha = 6$ (see **Fig. 9c**). Fingering instability forms at the exposed surface of the hydrogel sample while the exposed surface of the rubber sample remains uniform circular shape with negligible undulations. The normalized nominal stress S / μ in Ecoflex rubber is much larger than that in hydrogel sample, which manifests the effect from material-stiffening as well (see **Fig. 9d**).

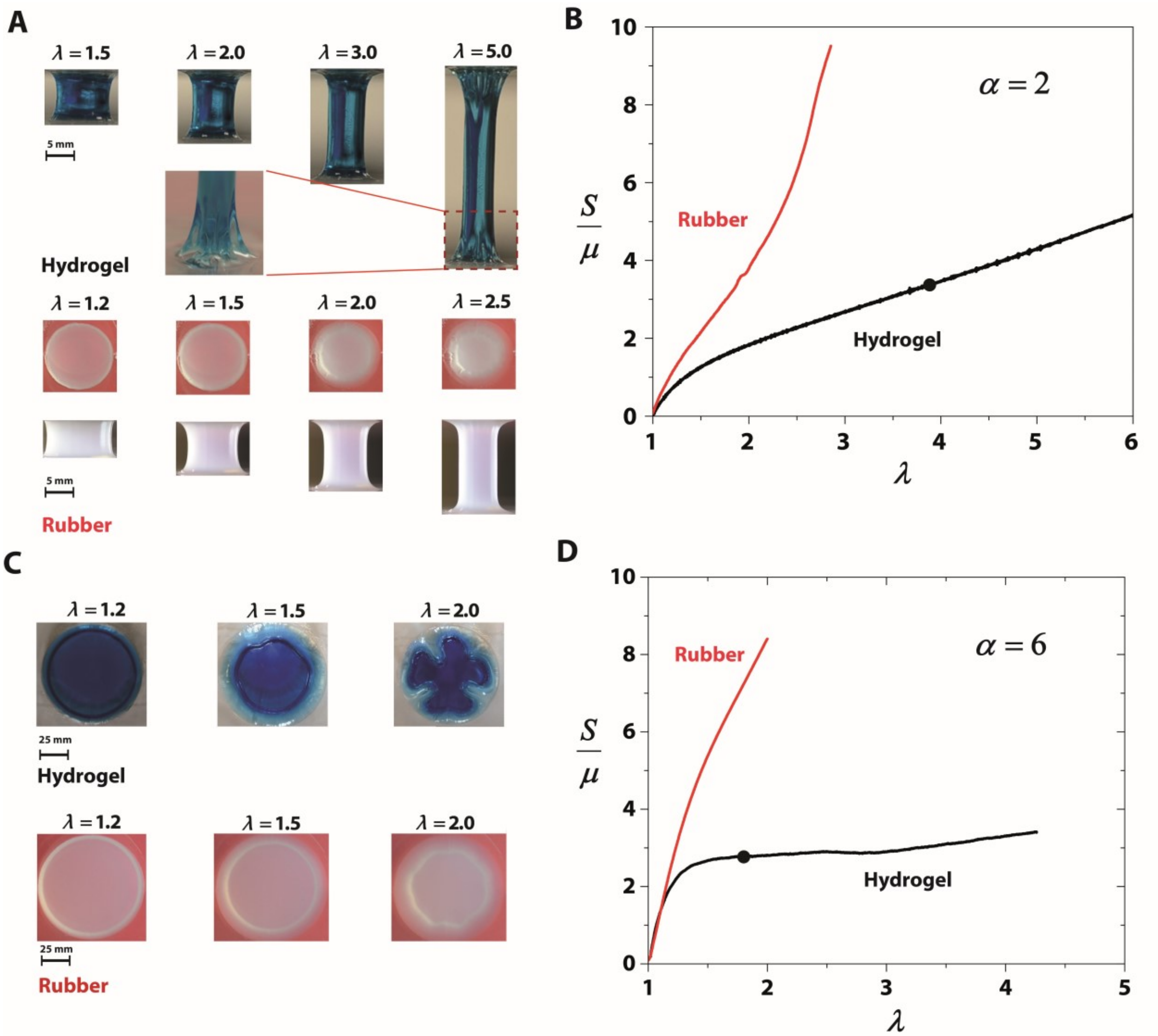

Figure 9. Experimental validation of the suppression of fingering and fringe instability in a stiffening layer. a) The evolution of the deformation in a hydrogel layer and rubber layer with aspect ratio of $\alpha = 2$ and b) corresponding applied stress-stretch curves. c) The evolution of the deformation in hydrogel layer and rubber layer with aspect ratio of $\alpha = 6$ and d) corresponding applied stress-stretch curves. Dots represent the onset of the instabilities.

7. Concluding remarks

In this paper, we explore the effect of material-stiffening on the onset of both fringe and fingering instabilities and stress vs. stretch relations. We show that for a layer with early stiffening, the local large deformation for instability development can be highly inhibited and both fringe and fingering instabilities can be delayed and even fully suppressed. In addition, we show the transition of stress vs. stretch relation from non-monotonic to monotonic with decreasing J_m . Most tough biological tissues indeed show stress-stretch curves with J-shape owning to the hierarchical integration of the strong coil-shape collagen and the surrounding soft matrices (Lin et al., 2014b; Motte and Kaufman, 2013). The systematic understanding of the material-stiffening on the effect of elastic instabilities in confined elastic layers may reveal the underlying toughening mechanisms, which the biological tissues (e.g. cartilage, ligament and mussel thread) adopt in nature to avoid these instabilities for long-term functionality. Moreover, the findings in this paper can evoke the need to design hydrogel-based composite structures (Huang et al., 2017; Lin et al., 2014a; Tummala et al., 2017), which can mimic the nature's strategy and as a result exhibit ultra-robust performances.

Acknowledgments

S. Lin acknowledges the online resources of VUMAT from Prof. Shawn Chester's group website. S. Lin acknowledges the helpful discussion from Prof. Tal Cohen at MIT. The work is supported by NSF (CMMI-1661627), ONR (N00014-17-1-2920) and MIT Institute for Soldier Nanotechnologies. H.Y. acknowledges the financial support from Samsung Scholarship.

Appendix A. Theoretical analysis for the onset of fingering and fringe instability in non-stiffening layers.

In previous paper, we derive the theoretical analysis for deformation field and perform linear perturbation for the onset of fingering and fringe instability in non-stiffening layers (Lin et al., 2017). We make a single assumption that any horizontal plane at the un-deformed state remains planar upon deformation. The displacement field in the cylindrical elastic layer can be specified as $u_R\left(\bar{R},\bar{Z}\right)=\bar{R}u_1\left(\bar{Z}\right)$ and $u_Z\left(\bar{Z}\right)=u_2\left(\bar{Z}\right)$. The deformation gradient in the layer can be expressed as:

$$\mathbf{F}=\begin{bmatrix}\lambda_{rR} & 0 & \gamma_{rZ}\\ 0 & \lambda_{\theta\Theta} & 0\\ 0 & 0 & \lambda_{zZ}\end{bmatrix}, \tag{A1}$$

with $\lambda_{rR}=\lambda_{\theta\Theta}=1+\frac{1}{D/2}u_1$, $\lambda_{zZ}=1+\frac{1}{H/2}u_2'$ and $\gamma_{rZ}=\frac{1}{H/2}\bar{R}u_1'$. For a non-stiffening material with the strain energy density function $\psi=\frac{\mu}{2}\left[\mathrm{tr}\left(\mathbf{F}^{\mathrm{T}}\mathbf{F}\right)-3\right]$, the nominal stress tensor $\mathbf{S}$ is expressed through $\mathbf{S}=\mu\mathbf{F}-p^*\mathbf{F}^{-\mathrm{T}}$, where p^* is the Lagrange multiplier to enforce the incompressibility and $\bar{p}=p^*/\mu$ is the corresponding dimensionless form. By enforcing the equilibrium equation $\mathrm{Div}\,\mathbf{S}=\mathbf{0}$ with boundary conditions that $\mathrm{d}u_1/\mathrm{d}\bar{Z}\,|_{\bar{Z}=0}=0$, $u_1(\bar{Z}=\pm 1)=0$, $u_2(\bar{Z}=0)=0$ and traction free at the middle plane, the deformation field and Lagrange multiplier in the elastic layer can be analytically solved as:

$$u_1(\bar{Z})=\frac{D}{2}\left[\frac{\cosh(\kappa\bar{Z})}{\cosh(\kappa)}-1\right], \tag{A2a}$$

$$u_2(\bar{Z})=\frac{H}{2}\left[\frac{\sinh(2\kappa)}{2\kappa}\frac{\tanh(\kappa\bar{Z})}{\tanh(\kappa)}-\bar{Z}\right], \tag{A2b}$$

$$\bar{p}=\frac{1}{2}\left(\frac{\cosh^4\kappa}{\cosh^4\left(\kappa\bar{Z}\right)}-\cosh^4\kappa\right)+\frac{\kappa^2\alpha^2}{2}\left(\bar{R}^2\frac{\cosh^2\left(\kappa\bar{Z}\right)}{\cosh^2\kappa}-\frac{1}{\cosh^2\kappa}\right)+\frac{1}{\cosh^2\kappa}. \tag{A2c}$$

where κ is an internal loading parameter which is correlated with the applied stretch through

$$\lambda=\frac{\sinh(2\kappa)}{2\kappa}. \tag{A3}$$

We further perform perturbation on both deformation field and Lagrange multiplier with first order perturbation as $\mathbf{x}=\left(\mathbf{x}\right)^0+\varepsilon\tilde{\mathbf{x}}$ and $\bar{p}=\left(\bar{p}\right)^0+\varepsilon\tilde{p}$, where ε is a dimensionless small parameter, $\left(\mathbf{x}\right)^0=u_R\mathbf{e}_\mathbf{R}+u_z\mathbf{e}_\mathbf{Z}$ and $\left(\bar{p}\right)^0=\bar{p}$ are the un-perturbed solutions in Eq. (A2), $\tilde{}$ and $\tilde{}$ are perturbed fields following the forms:

$$\tilde{} \qquad u_1(Z)\cos\left(\omega\Theta\right)\mathbf{e}_R+A_2(R)u_1(Z)\sin\left(\omega\Theta\right)\mathbf{e}_\Theta+A_3(R)u_2(Z)\sin\left(\omega\Theta\right)\mathbf{e}_Z, \tag{A4}$$

$$\tilde{p}=A_4(Z,R)\cos(\omega\Theta), \tag{A5}$$

where A_i ($i=1,2,3,4$) are the amplitudes of perturbation. Therefore, the perturbed deformation gradient may write as $\mathbf{F}=\left(\mathbf{F}\right)^0+\varepsilon\mathrm{Grad}\tilde{}$, where $\left(\mathbf{F}\right)^0$ is the un-perturbed deformation gradient at base state expressed in Eq. (A2). By inserting the perturbed displacement field, the deformation gradient reads as:

$$\mathbf{F}=\begin{bmatrix}\lambda_{rR}+\varepsilon A_1'u_1\cos(\omega\Theta) & -\varepsilon\frac{A_1\omega+A_2}{R}u_1\sin(\omega\Theta) & \gamma_{rZ}+\varepsilon A_1u_1'\cos(\omega\Theta)\\ \varepsilon A_2'u_1\sin(\omega\Theta) & \lambda_{\theta\Theta}+\varepsilon\frac{A_2\omega+A_1}{R}u_1\cos(\omega\Theta) & \varepsilon A_2u_1'\sin(\omega\Theta)\\ \varepsilon A_3'u_2\cos(\omega\Theta) & -\varepsilon\frac{A_3\omega}{R}u_2\sin(\omega\Theta) & \lambda_{zZ}+\varepsilon A_3u_2'\cos(\omega\Theta)\end{bmatrix}. \tag{A6}$$

The incompressibility of the elastic layer is enforced by $\det\mathbf{F}=1$, which implies:

$$\lambda_{zZ}A_1'u_1+\lambda_{zZ}\frac{A_2\omega+A_1}{R}u_1-\gamma_{rZ}A_3'u_2+\lambda_{rR}A_3u_2'=0. \tag{A7}$$

The perturbation in deformation gradient will further induce a perturbation in nominal stress which results in the nominal stress reading as $\mathbf{S}/\mu = (\mathbf{S})^0/\mu + \varepsilon\,\tilde{}$. Here, $\tilde{\mathbf{S}}$ is the perturbed normalized nominal stress writing as $\tilde{} \quad \tilde{} \quad)^0 (\mathbf{F})^{0-\mathrm{T}} - \bar{p}\mathbf{F}^{-\mathrm{T}} \big]$. A balance of the forces exerted on an element of the perturbed elastomer further leads to three equations of equilibrium through $\mathrm{Div}\,\tilde{\mathbf{S}} = 0$. The four unknown A_i ($i = 1,2,3,4$) can be fully specified by these three equations and the incompressibility condition in Eq. (8) with boundary conditions that the traction $\mathbf{t}_R = \mathbf{S}\cdot\mathbf{e}_R$ shall be zero at $\bar{R} = 1$. The four equations can be simplified by eliminating A_2 and A_4. Furthermore, we notice that fingering instability is an instability mode with $A_3 = 0$ and fringe instability with the layer's aspect ratio slightly smaller than the transition aspect ratio $\alpha_{fringe-fingering}$ between fingering instability and fringe instability is an instability mode with $A_3 \ll A_1$ and $A_3 \ll A_2$. Therefore, the only governing ODE to be solved is with respect to the amplitude along radius direction A_1 in the dimensionless form, reading:

$$\bar{R}^4 A_1^{(4)} + 6\bar{R}^3 A_1^{(3)} + \left(5 - 2\omega^2\right)\bar{R}^2 A_1'' - \left(2\omega^2 + 1\right)\bar{R}A_1' + \left(\omega^2 - 1\right)^2 A_1$$

$$- A_h^2 \bar{R}^2 \left[\bar{R}^2 A_1'' + 3\bar{R}A_1' - \left(\omega^2 - 1\right)A_1\right] = 0 \ , \tag{A8}$$

with $A_h = \sqrt{\dfrac{\kappa^2\alpha^2}{1-\lambda_{rR}}}$. By setting the boundary conditions of traction free at $\bar{R} = 1$, namely $\tilde{}$, $\tilde{}$ and $\tilde{}$, the two boundary conditions in the dimensionless form read as:

$$A_1^{(3)}(1) + 4A_1''(1) + \left[1 - 2\omega^2 - \zeta\omega^2 - A_h^2\right]A_1'(1) + \left[\omega^2 - 1 + \omega^2\kappa^2\alpha^2 - A_h^2\right]A_1(1) = 0, \tag{A9a}$$

$$A_1''(1) + \left(2 - \zeta\right)A_1'(1) + \zeta\left(\omega^2 - 1\right)A_1(1) = 0, \tag{A9b}$$

with

$$\zeta(\bar{Z}_0) = \frac{1}{2}\kappa^2\alpha^2 + \frac{1}{2}\lambda_{rR}^{-6} + C_3\lambda_{rR}^{-2}, \tag{A9c}$$

$$C_3 = \frac{1}{\cos^2\kappa}\left[1 - \frac{1}{2}\kappa^2\alpha^2\right] - \frac{1}{2}\cos^4\kappa. \tag{A9d}$$

The existence of the non-trivial solution for Eq. (A8) with two boundary conditions in Eq. (9) depends on whether the following equation has solution or not:

$$\left(l^2\omega^3 A_h + lA_h^3 - l^2\omega A_h\right)\frac{I_{\omega-1}(A_h)}{I_\omega(A_h)} - \left(2l\omega^2 A_h^2 + 2l^2\omega^4 - 2l^2\omega^2 + A_h^4\right)$$

$$+\left(2l\omega^2 + \omega A_h^2 - l\omega A_h \frac{I_{\omega-1}(A_h)}{I_\omega(A_h)}\right)\kappa^2\alpha^2 = 0, \tag{A10}$$

where $l = 1 + \zeta$.

By minimizing κ through ω at each plane, we can have the critical stretch λ_c, the critical number of undulations ω_c and the vertical location of the plane where the undulations initiate $\bar{Z}_0$. As shown in **Fig. 3**, the theoretical results for the critical stretch λ_c and the critical number of undulations ω_c are compared with simulation results, showing good agreement.

References

Benjamin, M., Toumi, H., Ralphs, J., Bydder, G., Best, T., Milz, S., 2006. Where tendons and ligaments meet bone: attachment sites ('entheses') in relation to exercise and/or mechanical load. Journal of anatomy 208, 471-490.

Biggins, J.S., Saintyves, B., Wei, Z., Bouchaud, E., Mahadevan, L., 2013. Digital instability of a confined elastic meniscus. Proceedings of the National Academy of Sciences 110, 12545-12548.

Chaudhury, M.K., Chakrabarti, A., Ghatak, A., 2015. Adhesion-induced instabilities and pattern formation in thin films of elastomers and gels. The European Physical Journal E 38, 1-26.

Creton, C., Ciccotti, M., 2016. Fracture and adhesion of soft materials: a review. Reports on Progress in Physics 79, 046601.

Crosby, A.J., Shull, K.R., Lakrout, H., Creton, C., 2000. Deformation and failure modes of adhesively bonded elastic layers. Journal of Applied Physics 88, 2956-2966.

Desmond, K.W., Zacchia, N.A., Waite, J.H., Valentine, M.T., 2015. Dynamics of mussel plaque detachment. Soft Matter 11, 6832-6839.

Gent, A., 1996. A new constitutive relation for rubber. Rubber chemistry and technology 69, 59-61.

Huang, Y., King, D.R., Sun, T.L., Nonoyama, T., Kurokawa, T., Nakajima, T., Gong, J.P., 2017. Energy-Dissipative Matrices Enable Synergistic Toughening in Fiber Reinforced Soft Composites. Advanced Functional Materials.

Lin, S., Cao, C., Wang, Q., Gonzalez, M., Dolbow, J.E., Zhao, X., 2014a. Design of stiff, tough and stretchy hydrogel composites via nanoscale hybrid crosslinking and macroscale fiber reinforcement. Soft matter 10, 7519-7527.

Lin, S., Cohen, T., Zhang, T., Yuk, H., Abeyaratne, R., Zhao, X., 2016. Fringe instability in constrained soft elastic layers. Soft Matter 12, 8899-8906.

Lin, S., Mao, Y., Radovitzky, R., Zhao, X., 2017. Instabilities in Confined Elastic Layers under Tension: Fringe, Fingering and Cavitation. Journal of the Mechanics and Physics of Solids.

Lin, S., Zhou, Y., Zhao, X., 2014b. Designing extremely resilient and tough hydrogels via delayed dissipation. Extreme Mechanics Letters 1, 70-75.

Liu, X., Tang, T.-C., Tham, E., Yuk, H., Lin, S., Lu, T.K., Zhao, X., 2017. Stretchable living materials and devices with hydrogel–elastomer hybrids hosting programmed cells. Proceedings of the National Academy of Sciences 114, 2200-2205.

Motte, S., Kaufman, L.J., 2013. Strain stiffening in collagen I networks. Biopolymers 99, 35-46.

Sharma, A., Licup, A., Jansen, K., Rens, R., Sheinman, M., Koenderink, G., MacKintosh, F., 2016. Strain-controlled criticality governs the nonlinear mechanics of fibre networks. Nature Physics.

Shull, K.R., 2002. Contact mechanics and the adhesion of soft solids. Materials Science and Engineering: R: Reports 36, 1-45.

Shull, K.R., Flanigan, C.M., Crosby, A.J., 2000. Fingering instabilities of confined elastic layers in tension. Physical review letters 84, 3057.

Silverman, H.G., Roberto, F.F., 2007. Understanding marine mussel adhesion. Marine Biotechnology 9, 661-681.

Tummala, G.K., Joffre, T., Rojas, R., Persson, C., Mihranyan, A., 2017. Strain-induced stiffening of nanocellulose-reinforced poly (vinyl alcohol) hydrogels mimicking collagenous soft tissues. Soft Matter 13, 3936-3945.

Waite, J.H., Andersen, N.H., Jewhurst, S., Sun, C., 2005. Mussel adhesion: finding the tricks worth mimicking. The journal of adhesion 81, 297-317.

Yuk, H., Lin, S., Ma, C., Takaffoli, M., Fang, N.X., Zhao, X., 2017. Hydraulic hydrogel actuators and robots optically and sonically camouflaged in water. Nature Communications 8.

Yuk, H., Zhang, T., Lin, S., Parada, G.A., Zhao, X., 2016a. Tough bonding of hydrogels to diverse non-porous surfaces. Nature materials 15, 190-196.
Yuk, H., Zhang, T., Parada, G.A., Liu, X., Zhao, X., 2016b. Skin-inspired hydrogel-elastomer hybrids with robust interfaces and functional microstructures. Nature Communications 7.
Zhao, B., Zeng, H., Tian, Y., Israelachvili, J., 2006. Adhesion and detachment mechanisms of sugar surfaces from the solid (glassy) to liquid (viscous) states. Proceedings of the National Academy of Sciences 103, 19624-19629.